Hindawi
Advances in Materials Science and Engineering
Volume 2018, Article ID 9409868, 10 pages
https://doi.org/10.1155/2018/9409868

*Research Article*

# Effects of Grain Orientation on Stress State near Grain Boundary of Austenitic Stainless Steel Bicrystals

**Fu-qiang Yang**,[1] **He Xue**,[2] **Ling-yan Zhao**,[1] **and Xiu-Rong Fang**[2]

[1] *School of Science, Xi'an University of Science and Technology, Xi'an 710054, China*
[2] *School of Mechanical Engineering, Xi'an University of Science and Technology, Xi'an 710054, China*

Correspondence should be addressed to Fu-qiang Yang; yang_afreet@163.com

Received 1 November 2017; Accepted 22 November 2017; Published 1 February 2018

Academic Editor: Pavel Lejcek

The stress state at the crack tip of structural components in nuclear power plants used in the SCC quantitative prediction models is based on the assumption that the polycrystalline material is isotropic and homogeneous at present. However, the crystals in polycrystalline materials are anisotropic with different orientations, which would induce a nonuniform stress to cause the initiation and propagation of SCC. By using a finite element method, the elastic responses of anisotropic behaviors of austenitic stainless steel bicrystals are studied. The results indicate that the stress distribution near GBs depends strongly on the crystal orientation. A larger Mises stress concentration exists on the GB with larger stiffness along the load direction. The Mises stress difference is higher in the bicrystal with bigger elastic modulus difference of two neighboring grains along the tensile axis. In the bicrystal with GB perpendicular to the tensile axis, the grain orientation has little effects on the Mises stress far from the GB in both grains. The strain inconsistency in bicrystals is affected by the mismatch of two neighboring grains. The larger the elastic modulus differences between two neighboring grains caused by misorientation, the larger the strain inconsistency in the bicrystal.

## 1. Introduction

Stress corrosion cracking (SCC) of structural components is one of the major factors that affect the reliability and integrity of the nuclear power plants (NPPs). Indeed, intergranular stress corrosion cracking (IGSCC) has occurred in many internal components made up of stainless steel, nickel alloy, and their weld metals [1–4]. The slip/dissolution-oxidation model has been widely accepted as a reasonable description of SCC in an oxygenated aqueous system [5–7]. In this model, SCC is regarded as the result of localized oxidation enhanced by stress/strain, and the crack tip strain rate is expressed as a unique parameter to cause the physical degradation of the interfacial film. Many attempts have been made to acquire the stress state of the crack tip due to its importance [6, 7]; however, the stress and strain are obtained macroscopically based on the assumption that the materials are isotropic and homogeneous in terms of elastic deformation when the materials have random crystallographic and morphologic texture. In fact, the crack tip stress state is significantly affected by the microstructure of materials due to the misorientation and anisotropic of each component crystal, and the crack tip would have a nonuniform stress at the microstructural level even under a uniform remote stress condition [8–11]. The inhomogeneity stress distribution caused by anisotropic of grains would play an important role in the initiation and propagation of SCC [12]. Researches have shown that the initiation of IGSCC in nickel alloys in high-temperature water greatly depends on inclination of the grain boundary (GB) to the tensile axis [13]; the cracks tend to be initiated easily at the GB whose inclination is perpendicular to the tensile axis and suggested that the local stress perpendicular to the GB governs the cracking behavior; this result seems to be consistent with the theory. However, other experiments and observations show that cracks could travel in different directions, such as at an angle perpendicular or even parallel to the applied load [14–16].

In order to precisely predict cracking characteristics, researchers have sought to acquire the local stress state near an individual GB with random shape and orientation of the crystal grains, and to find the driving force for cracking [17]. The test of bicrystals with a single symmetrical 111-tilt GB using the slow strain rate technique (SSRT) shows that the susceptibility to IGSCC depends on the misorientation rather than on the GB energy. The local stress concentration at large-angle GBs could be attributed to a high susceptibility to the IGSCC [18]. Single GBs in real alloys were also generated and monitored by using cantilevers manufactured by focused ion beam (FIB) and tested by nanoindentation, which was expected to provide a more accurate method of measuring the crack growth and investigate the dependence of SCC resistance of the single GB on GB character and composition [19–22]. However, it is difficult to manufacture a specific single GB with respect to the random orientation of neighboring grains and also to accurately measure the stress and strain distribution near the GB. Thus, a three-dimensional anisotropic finite element method (FEM) is performed in this paper to determine how the crystal orientation affects the stress state near the GB of the bicrystal.

## 2. Finite Element Model

*2.1. Geometry Model.* Two types of GBs are considered in bicrystals with respect to the relationship between the GB and tensile axis. The type-I GB is perpendicular to the tensile axis as shown in Figure 1, and the type-II GB is parallel to the tensile axis as shown in Figure 2. The average grain size of 316L stainless steel varies from 17 $\mu$m to 200 $\mu$m with different aging time, temperatures, and other factors in literature [23, 24]; the dimension of each component grain in the bicrystal with type-I GB is assumed to be $20\,\mu\text{m} \times 20\,\mu\text{m} \times 50\,\mu\text{m}$, and each grain in the bicrystal with type-II GB is of the dimension $10\,\mu\text{m} \times 20\,\mu\text{m} \times 50\,\mu\text{m}$ in this study.

*2.2. Material Propriety.* Stainless steel 316L is a polycrystalline material composed of austenitic crystal which has the face-centred cubic (FCC) configuration. The single crystal of 316L is orthotropic, and the elastic anisotropy is modeled using the elastic constants $d_{11} = 204.6$ GPa, $d_{12} = 137.7$ GPa, and $d_{44} = 126.2$ GPa [25]. When the crystallographic axial system coincides with the global coordinate, the elastic stress and strain relationship of the single crystal is described by the generalized Hooke's law:

$$\sigma = D\varepsilon, \tag{1}$$

where

$$\varepsilon = \{\varepsilon_{11}, \varepsilon_{22}, \varepsilon_{33}, \varepsilon_{12}, \varepsilon_{13}, \varepsilon_{23}\}, \tag{2}$$

$$\sigma = \{\sigma_{11}, \sigma_{22}, \sigma_{33}, \sigma_{12}, \sigma_{13}, \sigma_{23}\}, \tag{3}$$

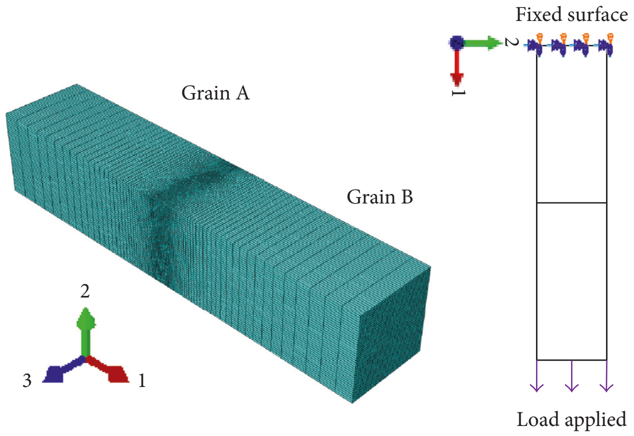

Figure 1: Type-I grain boundary: GB perpendicular to the tensile axis.

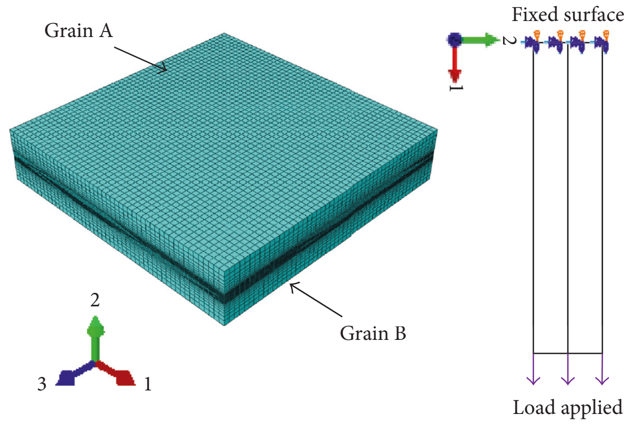

Figure 2: Type-II grain boundary: GB parallel to the tensile axis.

$$D = \begin{bmatrix} d_{11} & d_{12} & d_{13} & & & \\ d_{21} & d_{22} & d_{23} & & & \\ d_{31} & d_{32} & d_{33} & & & \\ & & & d_{44} & & \\ & & & & d_{55} & \\ & & & & & d_{66} \end{bmatrix}, \tag{4}$$

where $\sigma$ and $\varepsilon$ denote the stress tensor and strain tensor, respectively, and $D$ is the stiffness matrix. $d_{ij}$ $(i, j = 1, 2, \ldots, 6)$ is the elastic constant with $d_{11} = d_{22} = d_{33}$, $d_{44} = d_{55} = d_{66}$, and $d_{12} = d_{13} = d_{23} = d_{21} = d_{31} = d_{32}$.

In a polycrystalline material, the crystal orientation is random and always differs from the global coordinate. The stress and strain should be recalculated with the rotation stiffness matrix $D^{xyz}$ as

$$D^{xyz} = ADA^{T}, \tag{5}$$

where $A$ is the rotation matrix, which is given as

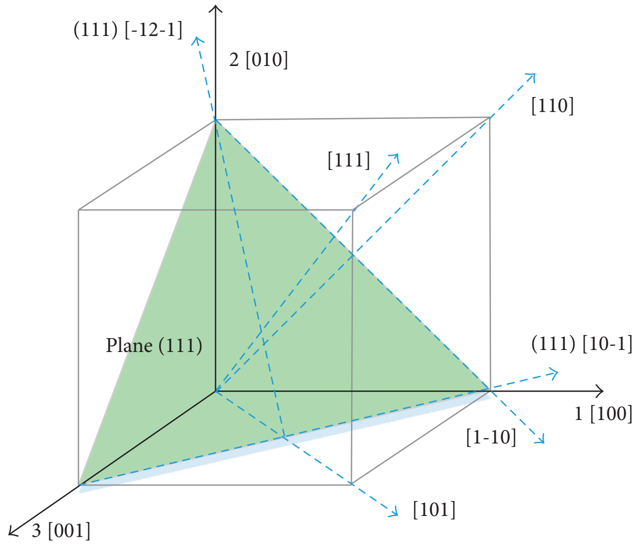

FIGURE 3: Selected crystallographic directions for analysis.

TABLE 1: Crystal orientations considered for grains.

| Grain type | $x'$ | $y'$ | $z'$ |
|---|---|---|---|
| Most compliant (MC) | [100] | [010] | [001] |
| Middle (MID) | [1-10] | [110] | [001] |
| Stiffness (ST) | [10-1] | [-12-1] | [111] |

TABLE 2: Incompatibility bicrystal models with three types of GBs.

| Incompatibility models | Grain A | Grain B |
|---|---|---|
| Model I | MC | MID |
| Model II | MC | ST |
| Model III | MID | ST |

$$A = \begin{bmatrix} l_1^2 & m_1^2 & n_1^2 & 2l_1m_1 & 2l_1n_1 & 2m_1n_1 \\ l_2^2 & m_2^2 & n_2^2 & 2l_2m_2 & 2l_2n_2 & 2m_2n_2 \\ l_3^2 & m_3^2 & n_3^2 & 2l_3m_3 & 2l_3n_3 & 2m_3n_3 \\ l_1l_2 & m_1m_2 & n_1n_2 & l_1m_2+l_2m_1 & l_1n_2+l_2n_1 & m_1n_2+m_2n_1 \\ l_1l_3 & m_1m_3 & n_1n_3 & l_1m_3+l_3m_1 & l_1n_3+l_3n_1 & m_1n_3+m_3n_1 \\ l_2l_3 & m_2m_3 & n_2n_3 & l_2m_3+l_3m_2 & l_2n_3+l_3n_2 & m_2n_3+m_3n_2 \end{bmatrix}, \tag{6}$$

where $l_i$, $m_i$, and $n_i$ ($i = 1, 2$, and $3$) are the direction cosines of $X$, $Y$, and $Z$ axes between the global coordinate and crystal coordinate.

The elastic modulus $E$, Poisson's ratio $\mu$, and shear modulus $G$ are equal, respectively, in the three main axes, and they can be calculated by elastic constants:

$$d_{11} = \frac{(1-\mu)}{(1-2\mu)(1+\mu)}E, \tag{7}$$

$$d_{12} = \frac{\mu}{(1-2\mu)(1+\mu)}E, \tag{8}$$

$$d_{44} = G. \tag{9}$$

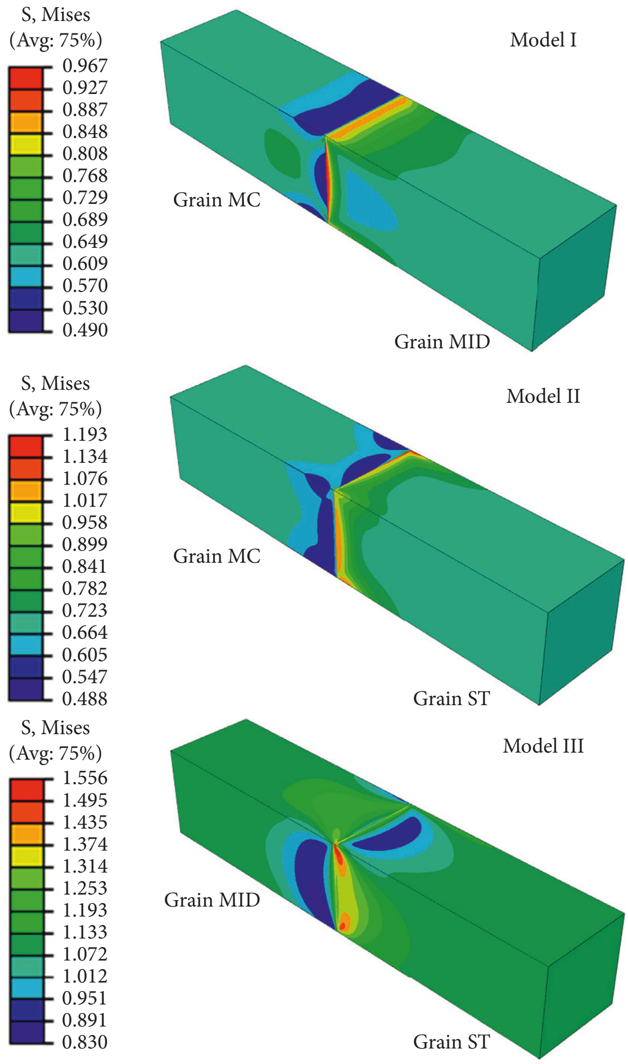

FIGURE 4: Mises stress (GPa) distribution on three incompatibility bicrystal models.

By substituting $d_{11}$, $d_{12}$, and $d_{44}$ into (7)–(9), it can be obtained that $E = 94.06$ GPa, $G = 126.2$ GPa, and $\mu = 0.402$.

The elastic modulus of the single crystal in <110> and <111> crystal orientations can be described with $E$, $G$, and $\mu$ in the three main axes as

$$\frac{1}{G} = \frac{4}{E_{110}} - \frac{2-2\mu}{E}, \tag{10}$$

$$\frac{1}{G} = \frac{3}{E_{111}} - \frac{1-2\mu}{E}. \tag{11}$$

According to (10) and (11), the elastic modulus along <110> and <111> orientations is $E_{110} = 193.81$ GPa and $E_{111} = 299.77$ GPa, respectively. The highest elastic stiffness is along the <111> orientation, and the lowest stiffness is along the <100> orientation, as shown in Figure 3. For different crystallographic directions, $E_{111} > E_{110} > E_{100} = E$.

Considering the relationship between [100], [110], and [111] orientations and the tensile axis, three types of grains

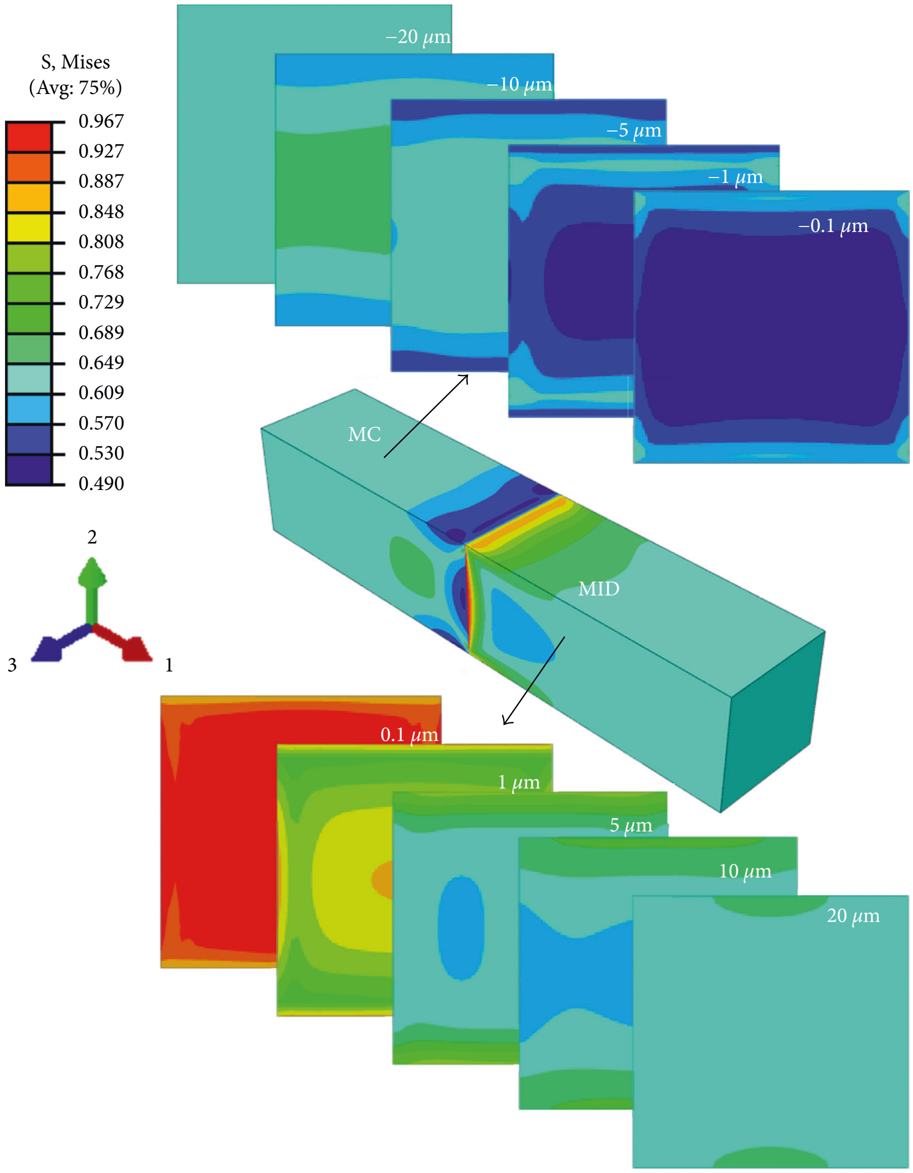

Figure 5: Mises stress (GPa) distribution on different cross sections.

with different orientations were modeled to build bicrystals, as listed in Table 1. The most compliant (MC) grain orientation is coincided with the global coordinate, which indicates that the crystal orientations [100], [010], and [001] denote the crystal axes $x'$, $y'$, and $z'$, respectively. By rotating the grain around [001] orientation, the middle (MID) stiffness grain has the (001)-[1-10] orientation as the axis $x'$; thus, the (001)-[110] orientation aligns with the global axis $x$. The most stiffness (ST) grain has the [111] orientation, which aligns with the global axis $x$ by defining the (111)-[10-1] and (111)-[-12-1] orientations as the crystal axes $x'$ and $y'$, respectively. In the three different grain types, the planes perpendicular to the global coordinate axis $x$ are (100), (110), and (111) planes in MC, MID, and ST grains, respectively.

In order to deeply understand the GB characterization, three types of incompatibility bicrystal models were built by combining grains with different orientations mentioned above, as listed in Table 2. The orientation of each grain is defined in the finite element model by rotating the material coordinate.

*2.3. Boundary Condition and Loading Process.* The 8-node linear brick C3D8R element was used in the finite element model, and a fine mesh was carried out at GBs to acquire more accurate stress and strain. The surface perpendicular to direction 1 of grain A is fixed initially with $U_1 = U_2 = U_3 = 0$, followed by a constant displacement $U_1$ equal to 0.5 along direction 1 applied on the surface of grain B, and this causes a total stain of 0.5% along direction 1 for the whole bicrystal.

## 3. Results and Discussion

*3.1. Bicrystal with Type-I Grain Boundary.* The Mises stress distributions in different types of GBs and incompatibility models are shown in Figure 4, which illustrates that the heterogeneity of two adjacent grains will lead to a stress concentration at the GB and the largest stress exists in the grain with higher elastic modulus along the tensile axis. The Mises stress distributions near the GB are different in the three bicrystals, which depend on the crystallographic orientation of the two adjacent grains and GBs. The maximum Mises stress appears on the GB of model III bicrystal.

More intuitive stress distribution was shown in Figure 5, which illustrates the stress distribution on different cross sections of model I bicrystal. On the cross section ±1 $\mu$m apart from the GB, the Mises stress shows a plateau in the middle of the cross section and a high gradient close to the surfaces, and the Mises stress gradient is higher along axis 3 than axis 2. With the cross section away from the GB, the high-stress area in the cross section reduces, accompanied by the reduction of the Mises stress gradient. The stress inconsistency at the GB induced by misorientation disappears when the cross section is far from the GB.

Let $\bar{\varepsilon}_{x\mathrm{A}}$ and $\bar{\varepsilon}_{x\mathrm{B}}$ represent the average strain $\varepsilon_{xx}$ of component crystals A and B along axis 1 and let $\bar{\varepsilon}_{\mathrm{A}}$ and $\bar{\varepsilon}_{\mathrm{B}}$ represent the average strain of all elements in contact with the GB in component crystals A and B, respectively. The characteristic of deformation near the GB of three incompatibility bicrystal models was evaluated, as listed in Table 3. $\bar{\varepsilon}_{x\mathrm{A}}/\bar{\varepsilon}_{x\mathrm{B}}$ is bigger than 1, which shows that the average strain of grain A is higher than that of grain B, and the average strain on the GB of grain A is also higher than that of grain B as represented by $\bar{\varepsilon}_{\mathrm{A}}/\bar{\varepsilon}_{\mathrm{B}}$. This indicates that the strain in the softer component (grain A) is higher than that in the harder component (grain B). The values of $\bar{\varepsilon}_{\mathrm{A}}/\bar{\varepsilon}_{x\mathrm{A}}$ denote that the strain near the GB is lower than the average strain of this grain in the softer component, while the strain near the GB is higher than the average strain of this grain in the harder component as denoted by $\bar{\varepsilon}_{\mathrm{B}}/\bar{\varepsilon}_{x\mathrm{B}}$. The strain inconsistency between two neighboring grains and between the GB and the entire grain is affected by the mismatch of two neighboring grains. In model II bicrystal, the elastic modulus difference of two grains is the largest; thus, the strain inconsistency in this bicrystal is the most serious.

To study the stress state caused by misorientation between grain A and grain B, a stress concentration factor $\lambda$ is introduced to normalize the stress as

$$\lambda = \frac{\text{actual stress}}{\text{average absolute stress}}, \tag{12}$$

where the actual stress and average absolute stress are observed along two paths, as shown in Figure 6. Path 1 penetrates the GB from grain A to grain B and path 2 locates on the GB. The average absolute stress is calculated along path 1 and path 2, respectively.

TABLE 3: The comparison of strain in each grain of the incompatibility models.

| Model type | $\bar{\varepsilon}_{x\mathrm{A}}/\bar{\varepsilon}_{x\mathrm{B}}$ | $\bar{\varepsilon}_{\mathrm{A}}/\bar{\varepsilon}_{\mathrm{B}}$ | $\bar{\varepsilon}_{\mathrm{A}}/\bar{\varepsilon}_{x\mathrm{A}}$ | $\bar{\varepsilon}_{\mathrm{B}}/\bar{\varepsilon}_{x\mathrm{B}}$ |
|---|---|---|---|---|
| Model 1 (MC-MID) | 1.43 | 2.04 | 0.82 | 1.17 |
| Model II (MC-ST) | 1.57 | 2.65 | 0.79 | 1.33 |
| Model III (MID-ST) | 1.11 | 1.30 | 0.88 | 1.03 |

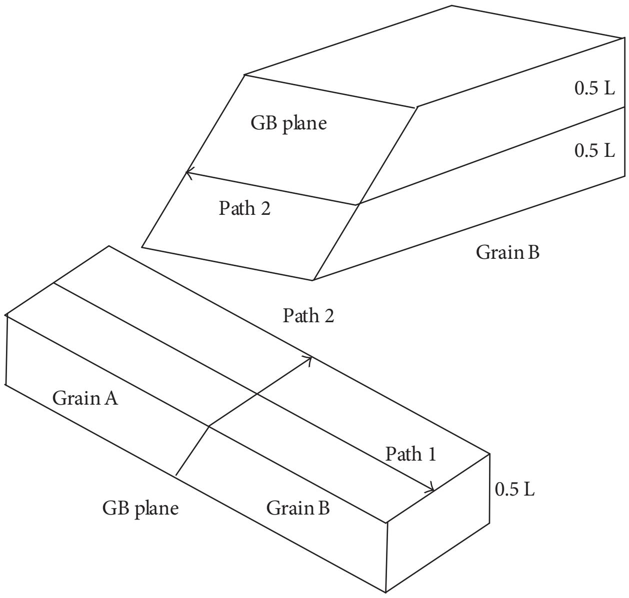

FIGURE 6: Locations of the two paths to determine the stress concentration factor.

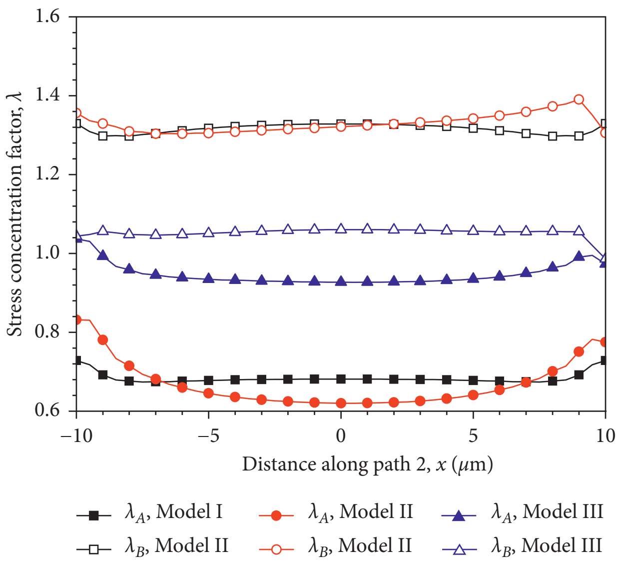

FIGURE 7: Mises stress concentration factor on the GB along path 1.

Figure 7 illustrates the stress concentration factor for path 1, and the Mises stress concentration factor is approximately flat in the middle and increases or decreases close to the edges in the softer and harder components, respectively. The Mises stress is higher in the harder component than in the softer component in each model. By defining the stress difference coefficient $\kappa$ as

$$\kappa = \frac{\sigma_{\mathrm{B}}}{\sigma_{\mathrm{A}}}, \tag{13}$$

where $\sigma_{\mathrm{A}}$ and $\sigma_{\mathrm{B}}$ are the stress in grain A and grain B, respectively, and the Mises stress difference for each model was demonstrated in Figure 8. The maximum stress

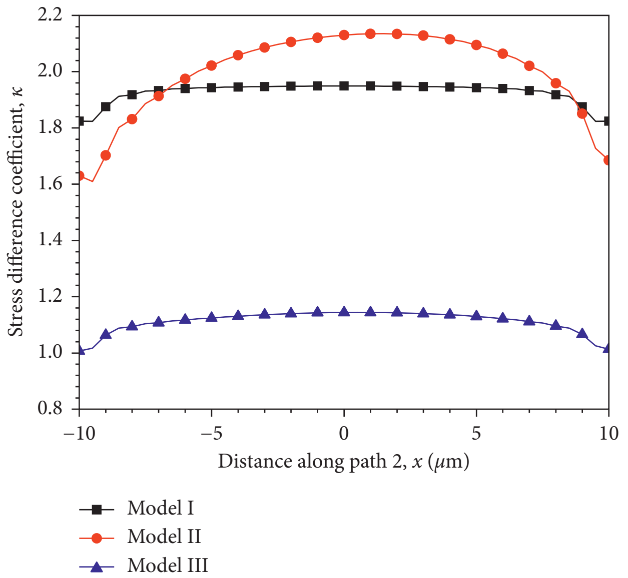

FIGURE 8: Mises stress difference coefficient on the GB along path 1.

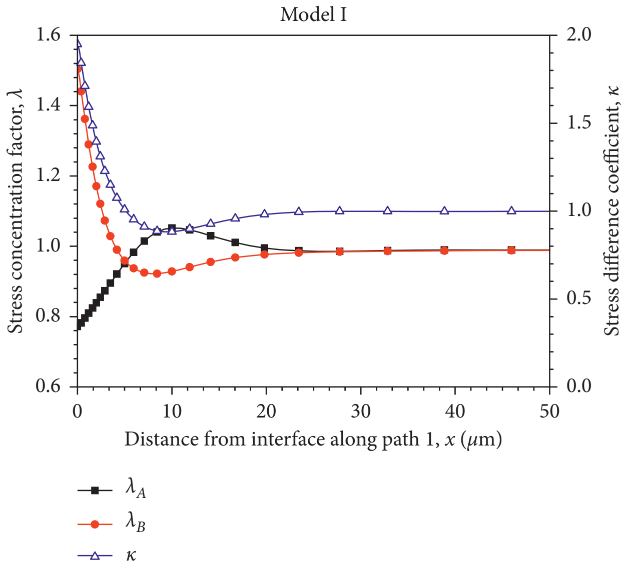

FIGURE 9: Mises stress concentration factor and Mises stress difference coefficient of model I along path 2.

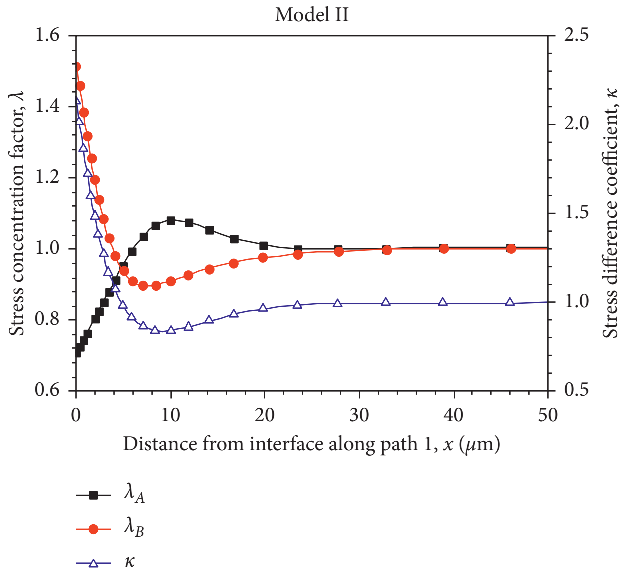

FIGURE 10: Mises stress concentration factor and Mises stress difference coefficient of model II along path 2.

difference appears at the middle of the GB and reduces gradually away from the middle in model II, which has the largest elastic modulus difference along the tensile axis, while the stress difference coefficient behaves constant in the middle and reduces slightly close to the edges in the other models. The minimum stress difference near the GB of model III has the smallest elastic modulus difference between the two adjacent grains along the tensile axis.

As shown in Figures 9 and 10, the Mises stress concentration factor and Mises stress difference coefficient for incompatibility model I and model II have the same tendency along path 2, which clearly demonstrates that a stress concentration exists near the GB and a uniform stress distribution in the regions is far from the GB in both grains. In the two harder components, the stress concentration factors are approximately 1.6 and 1.4, respectively, and both reduce to 1 far from the GB. In the softer grain near the GB, the stress concentration factor is below 1 and increases to 1 far from the GB. The stress difference coefficient for both the models is higher at the GB and reduces to 1 far from the GB.

Figure 11 shows a different Mises stress distribution in both grains along path 2 in model III. Stress concentration exists at the GBs in both grains, and it is more significant in the harder grain. The elastic modulus difference in model III is the smallest; thus, the stress difference coefficient at the GB is the lowest and also reduces to 1 far from the GB. This indicates that the stress far away from the GB equals each other and is not affected by the grain orientation and GB. Thus, the Mises stress in the middle of grains may be equal if the adjacent grain size is larger enough.

*3.2. Bicrystal with Type-II Grain Boundary.* As shown in Figure 12, a big difference of the Mises stress distribution on the GB of grain B for type-II bicrystal is observed, which intuitively demonstrates the misorientation effects of two adjacent grains. The Mises stress along path 1 increases with a large gradient initially and then reaches a plateau with a small gradient. The Mises stress on path 2 seems to be equal in the central region and has a small gradient close to the edges. The stress difference coefficient along path 2 in Figure 13 shows that a stress concentration exists at the GB and the most serious stress concentration appears in model II bicrystal, which has the largest elastic modulus difference along the load axis. The stress concentration is the smallest in model III bicrystal with the smallest elastic modulus difference along the load axis.

The stress components $\sigma_{22}$, $\sigma_{21}$, and $\sigma_{23}$ on the GB along path 2 are further studied. The tensile stress component $\sigma_{22}$ is perpendicular to the GB plane, which could lead to the fracture of bicrystal at GB. The shear stress components $\sigma_{21}$

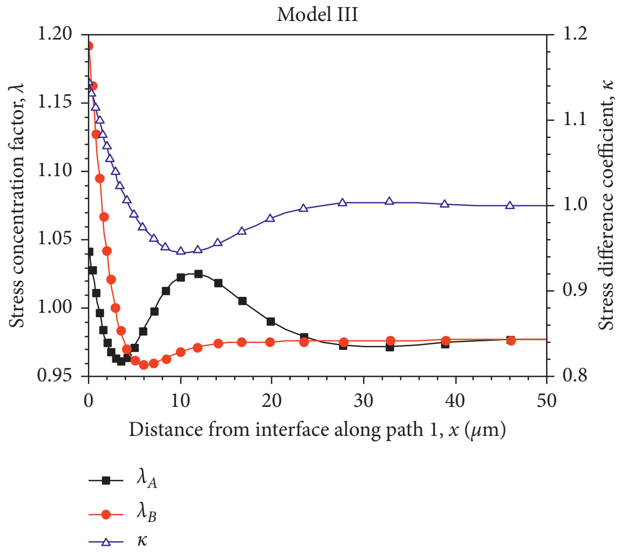

Figure 11: Mises stress concentration factor and Mises stress difference coefficient of model III along path 2.

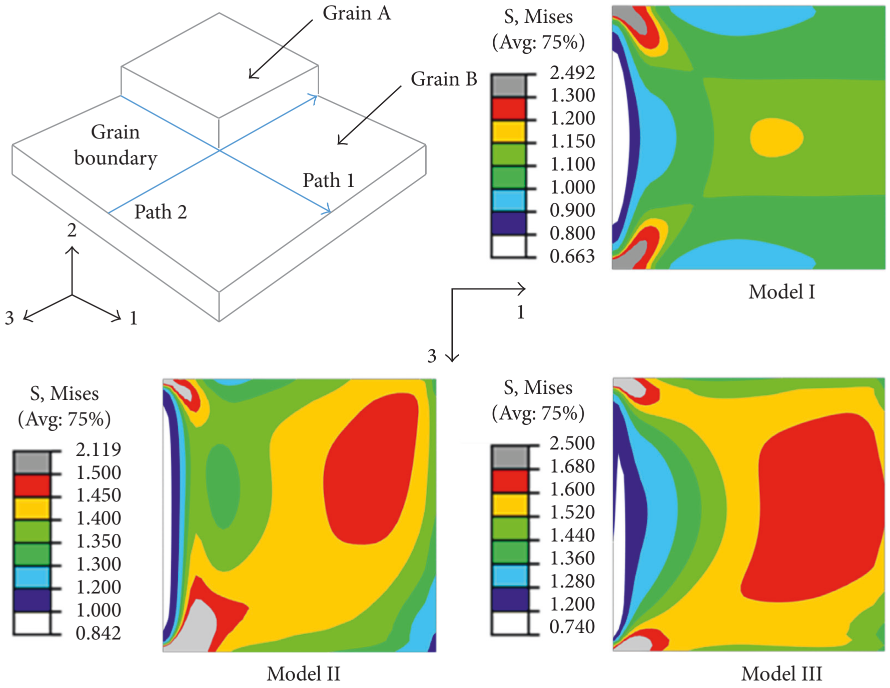

Figure 12: Mises stress distribution on the GB of grain B for type-II bicrystal.

and $\sigma_{23}$ are tangent to the GB plane, which may lead to the shear failure of the GB. The shear stress components $\sigma_{21}$ and $\sigma_{23}$ are considered to be shear stress $\tau$ tangent to the GB plane as

$$\tau = \sqrt{\sigma_{21}^2 + \sigma_{23}^2}. \tag{14}$$

Figure 14 illustrates the stress component distribution on the GB of model I bicrystal. As shown in Figure 14(a), the tensile stress in grain A fluctuates in a small range of ±4 MPa, and the shear stress also fluctuates slightly around 13 MPa in the central region and increases to 85 MPa rapidly close to the edges. The shear stress is larger than the tensile stress in grain A, especially close to the edges. The angle between shear stress and load direction varies from −135° to +135° at different positions. The angle is about ±135° close to the edges, which indicates that the shear stress is almost parallel to the [101] and [10-1] directions on the slip plane {111}. The angle equal to 0° or ±180° indicates that the stress component $\sigma_{23}$ is zero, while the angle equal to ±90° indicates that the stress component $\sigma_{21}$ is zero. As shown in Figure 14(b), the tensile stress is

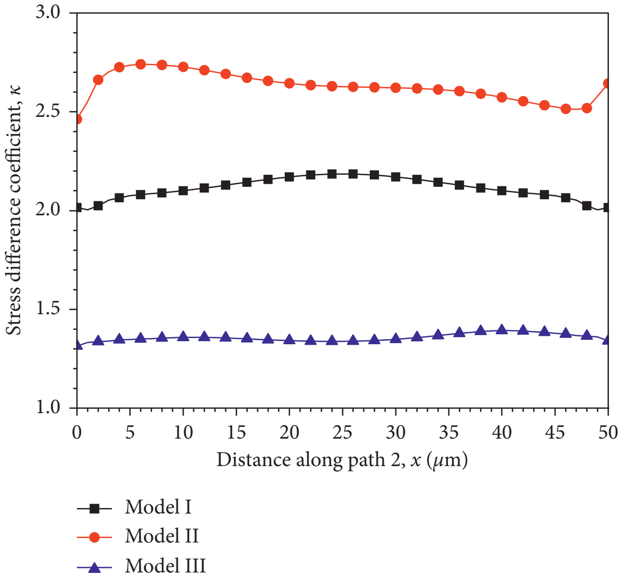

FIGURE 13: Mises stress difference coefficient along path 2.

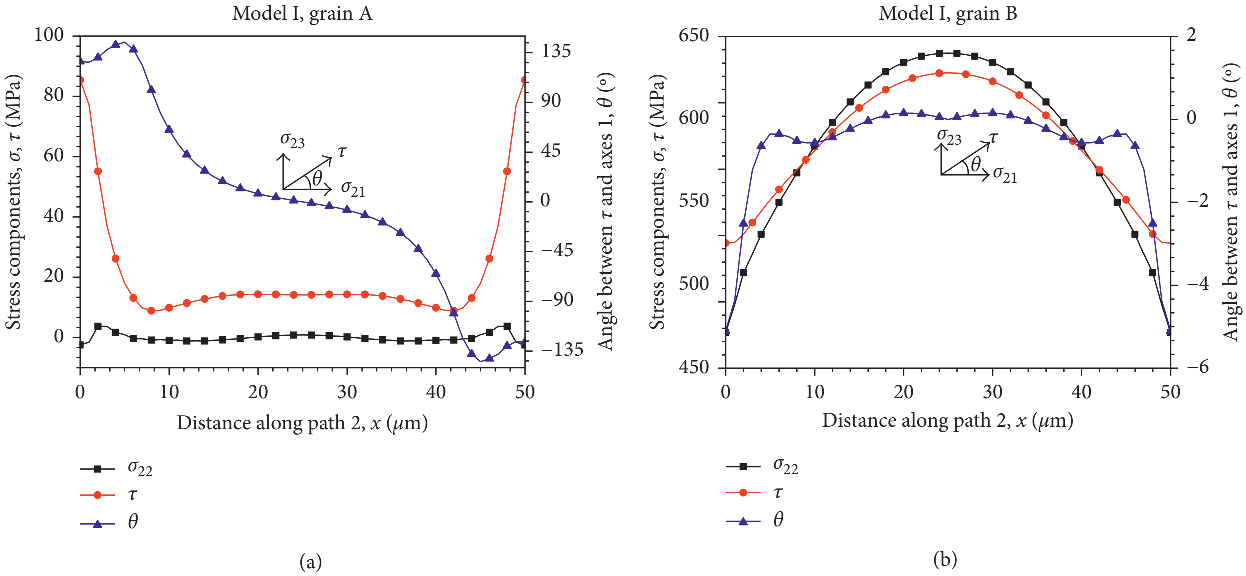

FIGURE 14: Stress components on model I GB: (a) grain A and (b) grain B.

larger than the shear stress in the central region, and then, they all reduce gradually from the central region to edges and result in a larger shear stress at edges. The stress components are much higher in grain B than in grain A, which demonstrates the stress concentration in grain B. The angle between shear stress and load direction is in a narrow range of [−1°, 6°], which indicates that the stress component $\sigma_{21}$ dominates the shear stress $\tau$ and the shear stress is almost parallel to the [110] direction. The symmetrical characteristic of stress components in grain A and grain B could be induced by the physical property symmetry of two grains with respect to tensile direction.

As shown in Figure 15(a), the tensile stress and shear stress along path 2 in grain A of model II are similar to those of model I, due to the same grain orientation of grain A in model II and model I. The tensile stress is flat with small values, and the shear stress is a little bigger than tensile stress in the central region and increases rapidly close to the edges. Due to the symmetry of grain A and the asymmetry of grain B, the stress components are approximately symmetry in grain A. As shown in Figure 15(b), the shear stress is about 2 times the tensile stress along path 2; thus, the shear failure appears. The angle between shear stress and tensile direction is in the range of [−150°, −135°], which is close to the angle between [012] direction and tensile direction on planes 1–3 or (-12-1).

A bigger difference between tensile stress and shear stress in grain A and grain B is observed in Figures 14 and 15, which indicates that a high stress concentration exists on the

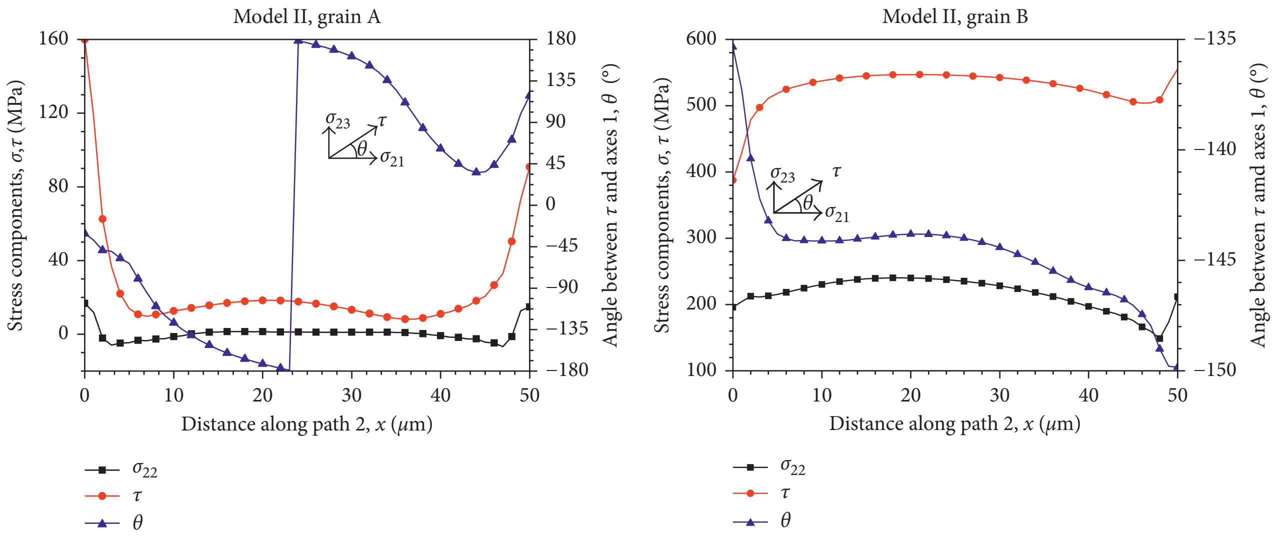

(a)

(b)

FIGURE 15: Stress components on model II GB: (a) grain A and (b) grain B.

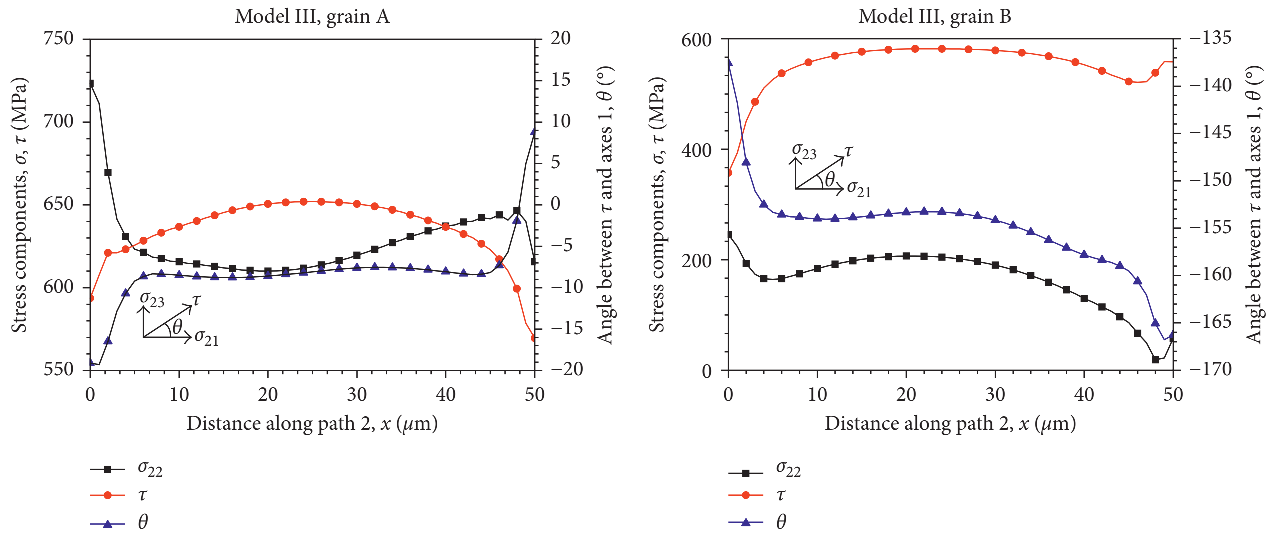

(a)

(b)

FIGURE 16: Stress components on model III GB: (a) grain A and (b) grain B.

GB of grain B, which has greater stiffness along the load direction in model I and model II. However, the situation is different in model III as shown in Figure 16, even the Mises stress is higher in grain B with greater stiffness, and the average tensile stress and shear stress in grain A are about 3.8 and 1.1 times than those in grain B, respectively.

## 4. Conclusions

A constitutive model has been presented to assess the elastic response of anisotropic behaviors of the austenitic stainless steel crystal. The FE method has been proposed to determine how the crystal orientation affects the stress state near the GB. The results indicate that the stress distribution near the GB depends strongly on the crystal orientation.

For bicrystals with the GB perpendicular or parallel to the tensile axis, elastic anisotropy causes additional stress in grain boundary regions and leads to the stress concentration on the GB of grains with larger stiffness along the load direction. The larger the elastic modulus difference of two neighboring grains along the tensile axis, the bigger the Mises stress difference appears at the GB.

With a GB perpendicular to tensile axes, a uniform Mises stress distribution in the region far from the GB in both grains is observed, which indicates that the grain orientation has little effects on the Mises stress distribution in this region. The Mises stress in the middle of adjacent grains may be equal if the grain size is larger enough.

The strain in the softer component is higher than that in the harder component; the strain near the GB is lower than the average strain of this grain in the softer component, while the strain near the GB is higher than the average strain of this grain in the harder component. The strain inconsistency between two neighboring grains and between the GB and the entire grain is affected by the mismatch of two neighboring grains. The larger the elastic modulus differences between two neighboring grains caused by misorientation, the larger the strain inconsistency in the bicrystals.

## Conflicts of Interest

The authors declare that there are no conflicts of interest regarding the publication of this paper. The authors confirm that the mentioned funding in the "Acknowledgments" section did not lead to any conflicts of interest regarding the publication of this manuscript.

## Acknowledgments

This work was supported by the National Natural Science Foundation of China (Grant nos. 51475362, 11502195, and 51775427), the Scientific Research Program Funded by Shaanxi Provincial Education Department (Grant no. 16JK1492), and the Start-up Foundation for Doctors of Xi'an University of Science and Technology (Grant no. 2016QDJ010).

## References

[1] P. M. Scott and C. Benhamou, "An overview of recent observation and interpretation of IGSCC in nickel base alloys in PWR primary water," NACE International, Lake Tahoe, NV, USA, 2001.

[2] P. M. Scott and P. Combrade, "On the mechanism of stress corrosion crack initiation and growth in alloy 600 exposed to PWR primary water," pp. 29–38, ANS, Stevenson, WA, USA, 2003.

[3] USNRC, *Crack in Weld Area of Reactor Coolant System Hot Leg Piping at V.C. Summer, NRC Information Notice*, U.S. Nuclear Regulatory Commission, Washington, DC, USA, 2000.

[4] R. M. Horn, G. M. Gordon, F. P. Ford, and R. L. Cowan, "Experience and assessment of stress corrosion cracking in L-grade stainless steel BWR internals," *Nuclear Engineering and Design*, vol. 174, no. 3, pp. 313–325, 1997.

[5] P. L. Andresen and F. P. Ford, "Fundamental modeling of environmental cracking for improved design and lifetime evaluation in BWRs," *International Journal of Pressure Vessels and Piping*, vol. 59, no. 1–3, pp. 61–70, 1994.

[6] T. Shoji, Z. Lu, and H. Murakami, "Formulating stress corrosion cracking growth rates by combination of crack tip mechanics and crack tip oxidation kinetics," *Corrosion Science*, vol. 52, no. 3, pp. 769–779, 2010.

[7] F. Q. Yang, H. Xue, L. Y. Zhao, and X. R. Fang, "A quantitative prediction model of SCC rate for nuclear structure materials in high temperature water based on crack tip creep strain rate," *Nuclear Engineering and Design*, vol. 278, pp. 686–692, 2014.

[8] K. Hashimoto and H. Margolin, "The role of elastic interaction stresses on the onset of slip in polycrystalline alpha brass-II. Rationalization of slip behaviour," *Acta Metallurgica*, vol. 31, no. 5, pp. 787–800, 1983.

[9] C. S. Nichols, R. F. Cook, D. R. Clarke, and D. A. Smith, "Alternative length scales for polycrystalline materials-I. Microstructure evolution," *Acta Metallurgica et Materialia*, vol. 39, no. 7, pp. 1657–1665, 1991.

[10] B. M. Schroeter and D. L. McDowell, "Measurement of deformation fields in polycrystalline OFHC copper," *International Journal of Plasticity*, vol. 19, no. 9, pp. 1355–1376, 2003.

[11] M. Kamaya and T. Kitamura, "Stress intensity factors of microstructurally small crack," *International Journal of Fracture*, vol. 124, no. 3-4, pp. 201–213, 2003.

[12] M. Kamaya and T. Kitamura, "A simulation on growth of multiple small cracks under stress corrosion," *International Journal of Fracture*, vol. 130, no. 4, pp. 787–801, 2004.

[13] M. Kamaya, "Influence of grain boundaries on short crack growth behaviour of IGSCC," *Fatigue and Fracture of Engineering Materials and Structures*, vol. 27, no. 6, pp. 513–521, 2004.

[14] Z. Lu, T. Shoji, F. Meng, Y. Qiu, T. Dan, and H. Xue, "Effects of water chemistry and loading conditions on stress corrosion cracking of cold-rolled 316NG stainless steel in high temperature water," *Corrosion Science*, vol. 53, no. 1, pp. 247–262, 2011.

[15] Z. Lu, T. Shoji, F. Meng et al., "Characterization of microstructure and local deformation in 316NG weld heat-affected zone and stress corrosion cracking in high temperature water," *Corrosion Science*, vol. 53, no. 5, pp. 1916–1932, 2011.

[16] T. Terachi, T. Yamada, T. Miyamoto, and K. Arioka, "SCC growth behaviors of austenitic stainless steels in simulated PWR primary water," *Journal of Nuclear Materials*, vol. 426, no. 1–3, pp. 59–70, 2012.

[17] B. Alexandreanu and G. S. Was, "The role of stress in the efficacy of coincident site lattice boundaries in improving creep and stress corrosion cracking," *Scripta Materialia*, vol. 54, no. 6, pp. 1047–1052, 2006.

[18] H. Miyamoto, H. Koga, T. Mimaki, and S. Hashimoto, "Intergranular stress corrosion cracking of pure copper <111> tilt bicrystals," *Interface Science*, vol. 9, no. 3–4, pp. 281–286, 2001.

[19] D. E. J. Armstrong, M. E. Rogers, and S. G. Roberts, "Micromechanical testing of stress corrosion cracking of individual grain boundaries," *Scripta Materialia*, vol. 61, no. 7, pp. 741–743, 2009.

[20] H. Dugdale, D. E. J. Armstrong, E. Tarleton, S. G. Roberts, and S. Lozano-Perez, "How oxidized grain boundaries fail," *Acta Materialia*, vol. 61, no. 13, pp. 4707–4713, 2013.

[21] A. Stratulat, D. E. J. Armstrong, and S. G. Roberts, "Micromechanical measurement of fracture behaviour of individual grain boundaries in Ni alloy 600 exposed to a pressurized water reactor environment," *Corrosion Science*, vol. 104, pp. 9–16, 2016.

[22] D. E. J. Armstrong, A. J. Wilkinson, and S. G. Roberts, "Micromechanical measurements of fracture toughness of bismuth embrittled copper grain boundaries," *Philosophical Magazine Letters*, vol. 91, no. 6, pp. 394–400, 2011.

[23] S. Kobayashi, R. Kobayashi, and T. Watanabe, "Control of grain boundary connectivity based on fractal analysis for improvement of intergranular corrosion resistance in SUS316L austenitic stainless steel random boundaries," *Acta Materialia*, vol. 102, no. 1, pp. 397–405, 2016.

[24] C. Y. Jeong, K. J. Kim, H. U. Hong, and S. W. Nam, "Effects of aging temperature and grain size on the formation of serrated grain boundaries in an AISI 316 stainless steel," *Materials Chemistry and Physics*, vol. 139, no. 1, pp. 27–33, 2013.

[25] H. M. Ledbetter, "Monocrystal-polycrystal elastic constants of a stainless steel," *Physica Status Solidi A: Applications and Materials Science*, vol. 85, no. 1, pp. 89–96, 1984.

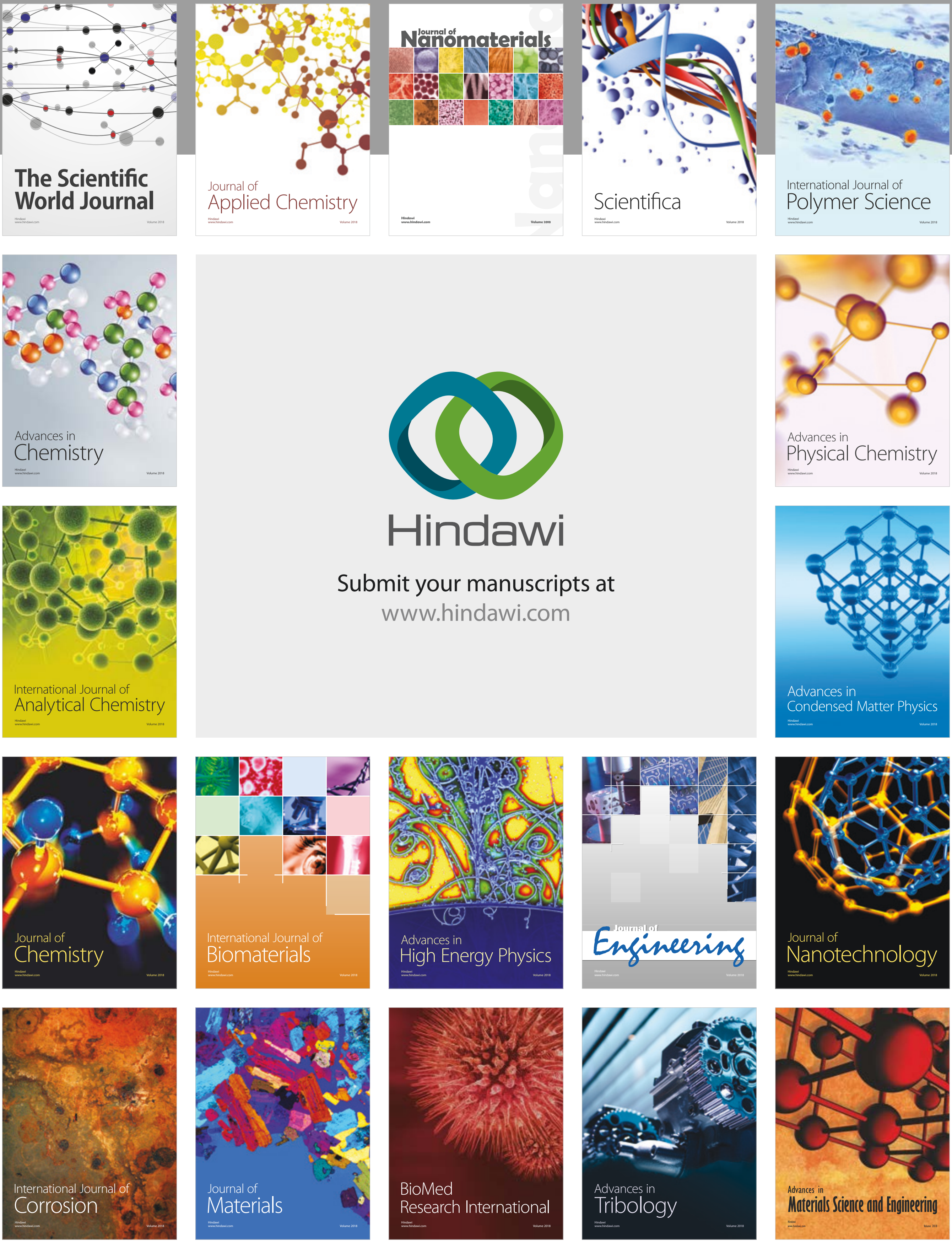
The Scientific World Journal
Journal of Applied Chemistry
Journal of Nanomaterials
Scientifica
International Journal of Polymer Science
Advances in Chemistry
Advances in Physical Chemistry
International Journal of Analytical Chemistry
Advances in Condensed Matter Physics
Journal of Chemistry
International Journal of Biomaterials
Advances in High Energy Physics
Journal of Engineering
Journal of Nanotechnology
International Journal of Corrosion
Journal of Materials
BioMed Research International
Advances in Tribology
Advances in Materials Science and Engineering